A Model-Driven Investigation into the Role of Wall Secondary Electron Emission in an Electron Cyclotron Resonance Magnetic Nozzle Thruster

IEPC-2024-432

Presented at the 38th International Electric Propulsion Conference, Toulouse, France
June 23-28, 2024

Ari J. Eckhaus* and Benjamin A. Jorns†
University of Michigan, Ann Arbor, MI, 48109, USA

The effects of wall material on the operation of a 30 W-class electron cyclotron resonance magnetic nozzle thruster are experimentally and computationally examined. Global performance as represented by thrust, specific impulse, and efficiency is experimentally measured as a function of input power and flow rate for operation with boron nitride, graphite, and aluminum walls. Comparison between the highest-performing material, boron nitride, and the lowest-performing material, aluminum, shows that specific impulse nearly doubles and total efficiency triples for otherwise identical operating conditions. A quasi-1D performance model is then regressed against these experimental results to infer key efficiency modes for the thruster including mass utilization and energy efficiency. It is found that the dominant driver for improved performance of boron nitride is a combination of an 18% increase in mass utilization efficiency and a 10% increase in energy efficiency, when compared to aluminum. These results are discussed in the context of simplified 0D scaling laws for the impact of secondary electron emission on particle and energy balance in the discharge. Higher plasma density within the thruster source region resulting from wall secondary electron emission is proposed as a possible mechanism for increasing mass utilization. The increased energy efficiency for boron nitride is a departure from the expectation that higher secondary electron emission results in greater power loss to the walls by lowering the sheath potential drop. This discrepancy is discussed in the context of cross-field diffusion within the source region, where boron nitride has improved confinement compared to the other materials.

I. Introduction

The role of donor electrons represents a gap in the current understanding of electron cyclotron resonance (ECR) devices. ECR technology is characterized by a plasma heating scheme that couples electromagnetic waves with an input frequency equal to the electron cyclotron frequency.[1] This facilitates efficient and rapid heating of the species. Because ECR heating is electrodeless and highly efficient, ECR sources are a promising candidate for low power electric propulsion (EP) applications, such as ECR magnetic nozzle thrusters. Despite the potential advantages of this scheme, however, there are aspects of ECR physics that remain poorly understood. One such phenomenon is the observed performance improvement when "donor electrons" are introduced via the walls of the ECR source by materials with high secondary electron yield (SEY).

The importance of wall material selection in ECR devices has been established empirically. Previously, it was determined that the stability of ECR ion sources improved when the walls were treated with a coating of material with high SEY.[2] In the context of ECR magnetic nozzles, experiments have shown a factor of 1.5 increase in thruster efficiency when the metallic walls of the thruster were coated in polyimide tape.[3] In

*Pre-Doctoral Candidate, Aerospace Engineering, aeckhaus@umich.edu
†Associate Professor, Aerospace Engineering

both cases, these studies suggested that secondary electron emission (SEE) from the walls was a potential driver for these performance improvements.

Two primary theories have been proposed as to how SEE from the walls affects performance of these devices. The first hypothesis suggests that donor electrons prevent electron starvation. Electron starvation occurs at high ratios of power to flow rate, when the heated electrons exit the source region more rapidly than they can ionize neutrals. As a result, ionization within the source region is inhibited, extinguishing the discharge. SEE may produce cold donor electrons, which originate from the walls and extend the effective residence time of the electron population in the source region. The increased residence time serves to maintain or even improve ionization. Improved ionization would be reflected in thruster performance by an increase in mass utilization, the efficiency at which inflowing propellant is converted into plasma. A second theory posits that secondary electrons alter the sheath dynamics in the source region. The modified sheath potential changes the radial wall losses, ultimately affecting performance of the device. This influence would be represented by variations in another efficiency mode of the thruster, the energy efficiency.

While these theories are qualitatively plausible, there has not yet been experimental validation of these hypotheses. This is in large part because a characterization of the effects of SEE would require probing of the source region to assess changes in the internal plasma dynamics. However, these probes are perturbative, meaning it would be difficult to accurately quantify the role of wall SEE.[4] Given the promise of ECR devices and their apparent dependence on wall material, there is a pressing need to bridge this knowledge gap and determine the mechanisms by which SEE influences the discharge of ECR magnetic nozzle thrusters.

The goal of this work is to address this need. Our approach is based on regressing a simplified quasi-1D model informed by global performance measurements. This model is then leveraged to infer key trends in the efficiency modes of the thruster to elucidate the influence of wall material choice. To this end, this paper is organized in the following way. In Sec. II, we present the global discharge model used in this effort. In Sec. IV, we discuss the experimental setup used to collect data during operating with various wall materials. In Sec. III, we present the statistical regression techniques used to calibrate the computational model on experimental data. In Sec. V, we compare the model results to experimental data and perform an efficiency breakdown with the regressed model results. In Sec. VI we attempt to interpret these results in the context of known models for how SEE influences particle and energy flux in low temperature discharges. Finally, we discuss the physical insights gained regarding the role of wall donor electrons.

II. ECR Global Discharge Model

In this section we first discuss the ECR magnetic nozzle principle of operation. We then examine the performance metrics used to quantify behavior of the ECR thurster. Finally, we provide an overview of the computational model utilized to capture global performance of the device.

A. Principle of Operation

Figure 1 shows the canonical cross section of an ECR magnetic nozzle thruster, which is characterized by a source region and a magnetic nozzle. In the source region, a steady magnetic field is applied, predominantly in the axial direction, by permanent magnets located behind the thruster. A centrally mounted antenna delivers electromagnetic (EM) waves, and a radial gas manifold provides propellant to the device. Downstream, the magnetic field diverges, creating the magnetic nozzle.

During operation, gas flows through the manifold, radially inward toward the source region. An EM wave is then injected to the thruster source region through the antenna, with the thruster walls acting as a waveguide. The frequency of the wave, ω_{EM}, is tuned to match the electron cyclotron frequency, ω_{ce}. This can be written as

$$\omega_{EM} = \omega_{ce} = \frac{eB}{m_e}, \tag{1}$$

with e being the fundamental charge, B denoting the magnitude of the magnetic field, and m_e representing the electron mass. When this condition is met, the electrons experience rapid and highly efficient heating due to cyclotron resonance. However, because the magnetic field strength varies with position, resonance only exists in a thin region of the source,[5] often referred to as the "resonance zone". The hot electrons collide with neutrals, causing ionization. The resulting plasma is contained by a back wall and a cylindrical source tube.

Because the electrons are less massive than ions, they are more mobile and will exit the source region first. These hot electrons travel downstream through the diverging magnetic nozzle. This bulk electron motion creates an ambipolar electric field, which accelerates the heavier ions downstream. Finally, at some downstream location the plasma detaches from the magnetic nozzle, allowing for thrust generation. Although a necessary mechanism for operation of all magnetic nozzle devices, the physics of magnetic detachment are poorly understood and are an active area of research.[6–10]

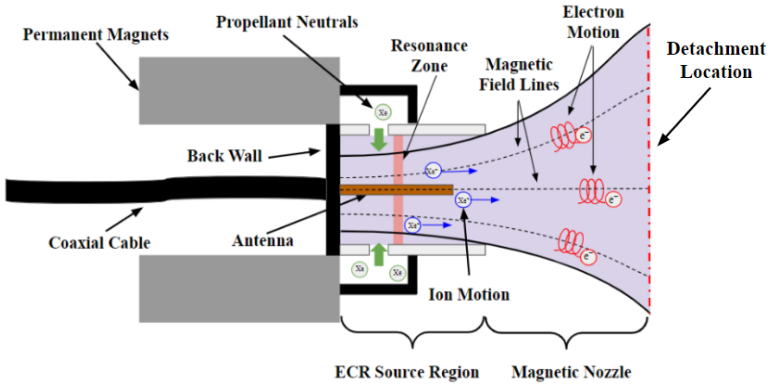

Figure 1. Notional ECR thruster geometry

B. Performance Quantification

Performance of EP systems is often discussed in two contexts: global performance metrics and sub-divided efficiency modes.[11] We outline both of these treatments in the following section.

1. *Key Performance Metrics*

The three most common global performance metrics are thrust, T, specific impulse, I_{sp}, and total efficiency, η. Thrust quantifies the total force generated by the thruster and is commonly measured directly during experiments using a thrust stand. Specific impulse is a metric for propellant efficiency of the system:

$$I_{sp} = \frac{T}{\dot{m}g}, \tag{2}$$

where $\dot{m}$ is the propellant mass flow rate and g is the standard acceleration of gravity at sea level. Finally, total efficiency represents the ratio of thrust generating jet power to absorbed power:

$$\eta = \frac{T^2}{2\dot{m}P_{abs}}, \tag{3}$$

where P_{abs} is the power absorbed by the plasma. We note here that this definition differs from the conventional formulation for thruster efficiency where the the total input power, P_{in}, is used in the denominator. The absorbed microwave power in practice can be different than the actual input power to the system, $P_{abs} = \eta_{rf} P_{in}$ where η_{rf} is the power coupling efficiency. This stems from possible reflection and mismatching effects. For the work we performed here, however, our focus is on the physics that results after the power is absorbed. We therefore adopted this modified definition.

2. *Efficiency Modes*

To capture loss mechanisms within the ECR thruster, it is useful to represent total efficiency as a product of multiple modes.[12,13] The break down we use follows the approach of Ref. 3, where total efficiency is expressed as

$$\eta = \eta_D \eta_m \eta_e. \tag{4}$$

In this expression, the parameter $\eta_D = cos(\theta_D)^2$, where θ_D is divergence angle, denotes the divergence efficiency of the thruster. This arises from the fact that the expanded plume will have non-axial components. We ultimately do not anticipate that this mode will be impacted by the internal material choice in the thruster, as the divergence is dictated by the downstream expansion of the magnetic field plume. We therefore do not further investigate this component in this work.

The efficiency mode, η_m, denotes the mass utilization:

$$\eta_m = \frac{\dot{m}_i}{\dot{m}}, \tag{5}$$

where $\dot{m}_i$ is the mass flow rate of ions out of the thruster. Physically, this represents the conversion of inflowing neutral gas to ions that can be accelerated for thrust generation. This factor is primarily impacted by ionization inside the source region.

The last mode in Eq. 4 is the energy efficiency given by

$$\eta_e = \frac{T^2}{2\eta_D \dot{m}_i P_{abs}}. \tag{6}$$

Physically, this parameter represents the conversion of absorbed power to the system to kinetic energy downstream of the thruster. It quantifies to the degree to which the flow is accelerated. Notably, this parameter does not include divergence effects, i.e. it only considers the energetics of the acceleration. Key factors that influence the energy efficiency include losses to the walls, inelastic losses from excitation and ionization, and frozen flow losses from incomplete expansion of the plume.

Given that the mass utilization and energy efficiency are directly tied to processes inside the source region, which in turn are impacted by wall material, we elect to focus on the characterization of the response of these modes in this work. To this end, we outline in the next section the model we employed to infer these contributions indirectly from experimental measurement.

C. Overview of ECR Thruster Model

To accurately capture the behavior of ECR thrusters in a computational model, it is necessary to simulate all interactions and processes described in Sec. A. The model used as the basis of our investigation is adapted from Lafleur's global discharge model for magnetic nozzles.[14] We overview the modeled processes and assumptions in the following sections.

1. Definition of Model Geometry and Processes

Similar to our previous discussion of ECR thruster operation, this model divides the thruster domain into two disparate regions: the ECR source and the downstream magnetic nozzle. This geometric description is summarized in Fig. 2. As can be seen, the geometry of the source region is characterized by the tube length, L_s, radius, R_s, and cross sectional area, A_0. Within the source region, the modeled processes are neutral injection, power input, electron heating, ionization, and recombination at the radial walls.

The transition from source to magnetic nozzle occurs at the nozzle's "throat", which is considered to be the downstream location where the source tube ends. In the magnetic nozzle, the plasma experiences an area expansion and acceleration. As shown in Fig. 2, this expansion is bounded by the grazing line, the outermost magnetic field line that "grazes" the walls of the source tube. At some point downstream, the accelerated plasma detaches from the magnetic nozzle and transitions to ballistic flow.

2. Model Assumptions

The quasi-1D discharge model we employ in this work has the following simplifying assumptions for the ECR discharge

1. Quasi-neutral plasma ($n_i = n_e$), where these denote plasma densities
2. Singly-charged species
3. Isothermal electrons

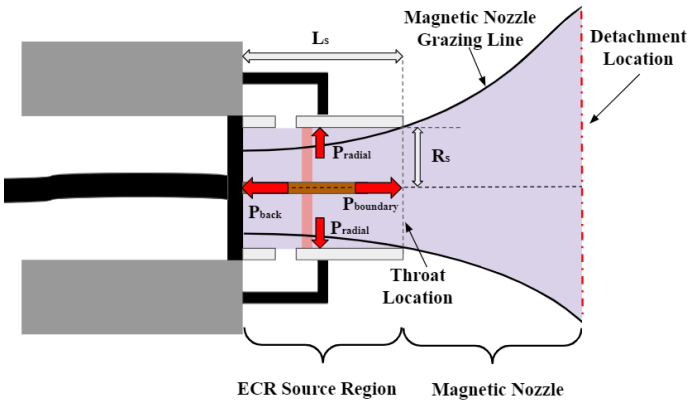

Figure 2. Global discharge model geometry

4. Cold ions ($T_i \ll T_e$), where these denote species temperatures
5. Maxwellian electron population for evaluating the reaction rates
6. Treats excitation as an average over transitions
7. Constant neutral velocity ($v_g = 225\frac{m}{s}$)
8. Neglect electron inertia
9. Sonic ions at the throat
10. Neglect ionization downstream of the source region
11. Ions stream to the walls at the Bohm speed (u_B)
12. Floating walls for source power balance
13. Neglect wall SEE.

Although this model explicitly neglects SEE from the walls, we are able to implicitly capture the effects of donor electrons through the model parameters. By regressing the model outputs to match experimental results of the thruster operating with various wall materials (see Sec. III), we can quantify changes to the model parameters, providing insight into the role of SEE.

In addition to these assumptions, a semi-empirical formula is employed to describe the radial variation in plasma density. It is assumed that the plasma within the source region has a self-similar profile given by

$$f(\rho) = n_p \left(1 - (1 - h_r^{\frac{1}{6}})\rho^2\right)^6, \tag{7}$$

where n_p denotes the plasma density on centerline, $\rho = r/R_s$ is the normalized radial position, and h_r is the ratio between the plasma density on centerline of the thruster and the wall. Following the work of Lafleur,[14] we adopt the same scaling law for this ratio:

$$h_r = \frac{0.4}{\sqrt{1 + c\frac{R_s}{r_{ci}}}}. \tag{8}$$

Here, $r_{ci} = \sqrt{\frac{m_i T_i}{eB_s^2}}$, is the ion cyclotron radius in the source region, m_i is the ion mass and B_s is the magnetic field strength at the resonance zone. The parameter, c, is a cross-field diffusion coefficient that depends on the plasma source. We ultimately treat this coefficient as a model parameter that we leverage to match experimental data (Sec. III).

Averaging the self-similar expression in Eq. 7 over the radius of the source region yields the result $\langle n_p \rangle = \beta n_p$ where

$$\beta = \frac{1}{7(1-h_r^{\frac{1}{6}})}\left(((1-h_r^{\frac{1}{6}})-1)^7+1\right). \tag{9}$$

This coefficient thus relates the average over the cross-section to the centerline density. We utilize this relationship in the formulation of a quasi-1D model for the source and nozzle.

3. Model Algorithm

Figure 3 summarizes the solution process of the model. As shown, the key model inputs include the design parameters dictating thruster geometry (source radius, length, and area) and operating condition (neutral mass flow rate and power coupling efficiency). Additionally, the model takes in model parameters of mass utilization efficiency, cross-field diffusion coefficient and ion Mach number at the detachment location, M_{det}. We note here that our treatment of the detachment Mach number as an input model parameter is a departure from Lafleur's implementation, where this quantity is calculated using an argument of conservation of magnetic flux at the exit plane.[14] We further discuss the handling of detachment Mach number as a model parameter in Sec. III. In the following, we review the key steps outlined in the flow chart process.

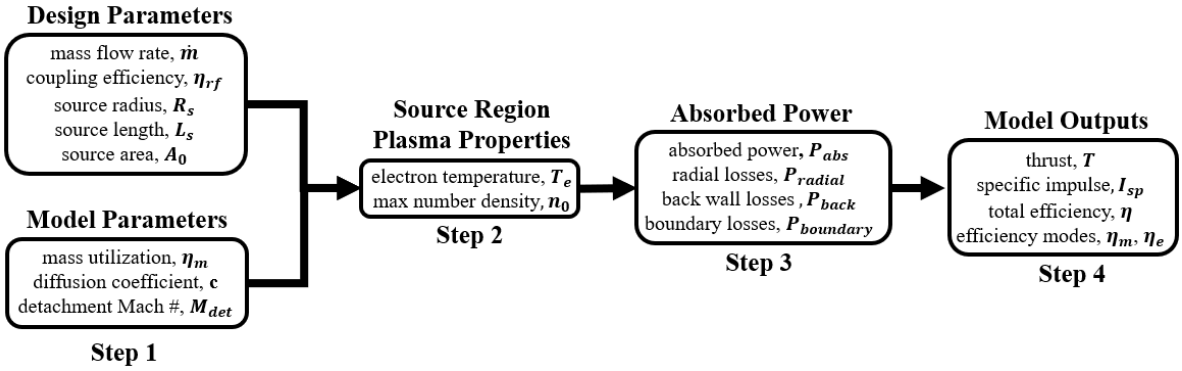

Figure 3. Global discharge model solution method

4. Evaluating the Source Region Plasma Properties

After defining the necessary design and model parameter inputs, we next evaluate the plasma properties inside the source region (step 2 in Fig. 3). To do so, the quasi-1D continuity and momentum equations are invoked subject to the assumptions defined in the previous section. This yields the non-dimensional equation for momentum balance in the system:

$$\zeta = -2 - \xi \ln\left(\frac{1-\xi}{1+\xi}\right) + 2\sqrt{1-\xi^2}\left[\operatorname{atan}\left(\frac{1-\xi}{\sqrt{1-\xi^2}}\right) - \operatorname{atan}\left(\frac{-1-\xi}{\sqrt{1-\xi^2}}\right)\right], \tag{10}$$

where we have the non-dimensional parameters:

$$\xi = \frac{\eta_m}{1-\frac{u_B}{K_{iz}}\left(\frac{2h_r v_g}{\beta R_s \Gamma_0}\right)}, \quad \zeta = \left(\frac{\Gamma_0 L_s}{v_g}\right)\frac{K_{iz}}{u_B} - \frac{2h_r L_s}{\beta R_s}. \tag{11}$$

Here $\Gamma_0 = \frac{\dot{m}}{m_i A_0}$ denotes the flux density of neutrals into the system, $u_B = \sqrt{\frac{eT_e}{m_i}}$ is the Bohm speed, and K_{iz} is the ionization rate, which is a function of electron temperature. In this work, we operate the ECR thruster on xenon propellant, which has a well-characterized ionization rate function.[11]

Implicitly, Eq. 10 depends on the electron temperature through the Bohm speed and ionization rate. All other parameters are dictated by inputs to the model, including the source radius, R_s, neutral flux density

into the system, Γ_0, neutral gas speed, v_g, source length, L_s, and mass utilization, η_m. Thus, for a given set of model parameters, Eq. 10 yields the electron temperature.

Once electron temperature is known, it is possible to extract the maximum plasma density on centerline in the source, n_0, from the definition of mass utilization. To this end, we first recognize that conservation of axial momentum in the source provides a relationship between this maximum density, where the plasma is stationary, to the density at the throat, n_t, where the plasma is accelerated to sonic speed, $\frac{n_t}{n_0} = 1/2$. In turn, invoking the definition of mass utilization and assuming ionization downstream of the source region is negligible, we find

$$n_0 = 2n_t = \frac{2\dot{m}\eta_m}{\beta u_B m_i A_0}. \tag{12}$$

Physically, this relationship reflects that as mass utilization and mass flow rate increase, so too does the density in the discharge

5. Absorbed Power

Armed with estimates for the electron temperature and density in the source region from Eq. 10 and 12 respectively, we evaluate the absorbed power to this system (step 3 in Fig. 3). This is given by evaluating the summation of all relevant channels for power flow in the system:

$$P_{abs} = [P_{back} + P_{radial} + P_{boundary}] \tag{13}$$

where P_{back} denotes the power lost to the upstream back wall of the thruster, P_{radial} denotes power loss to the radial wall, and $P_{boundary}$ represents power streaming through the throat of the system. Based on the work of Ref. 14, we can explicitly define these quantities in terms of the geometry and the evaluated density and temperature from the previous section. For the back wall losses, we assume that ions stream to the back wall at the Bohm speed. Under this assumption we find

$$P_{back} = \frac{1}{2} e\beta n_0 u_B A_0 (\varepsilon_c + \varepsilon_i + \varepsilon_{es}). \tag{14}$$

Here we have the average inelastic energy loss per unit mass of the electrons in the source:

$$\varepsilon_c = \epsilon_{iz} + \frac{K_{exc}}{K_{iz}} \epsilon_{exc}. \tag{15}$$

This loss term arises from inelastic collisions between neutrals and electrons that both ionize or excite neutrals. Terms $\epsilon_{iz} = 12.13$ eV and $\epsilon_{exc} = 8.32$ eV are the first ionization energy and average excitation energy for neutral xenon.[15] Loss term ε_i denotes the energy of ions fluxing to the sheath:

$$\varepsilon_i = \frac{Te}{2}. \tag{16}$$

This represents the ion kinetic energy at the sheath edge under the assumption that ions are accelerated to the Bohm speed. Similarly, ε_{es} represents the electron energy at the sheath edge:

$$\varepsilon_{es} = 2T_e + \frac{Te}{2} \ln\left(\frac{m_i}{2\pi m_e}\right). \tag{17}$$

The first term in this equation is the average electron energy in the plasma. The second term arises from the energy of electrons that overcome the sheath to reach the wall. In total, this represents the average energy that each electron removes from the plasma as it reaches the wall. The sheath potential used here holds for floating walls and neglects the effects of secondary electrons, which will modify the sheath potential and change the electron energy loss to the walls.[11,16] We note here again (see Sec. III) that although we neglect SEE explicitly in this formulation, there is a mechanism that can implicitly capture this effect on sheath losses, the parameter c (Eq. 8). Adjustments to this value can indirectly represent modifications to the sheath losses that are moderated by SEE.

The power lost to the radial wall is expressed as

$$P_{radial} = 2\pi R_s e h_r \left[\frac{n_0 L_s}{2\zeta\xi}\ln\left(\frac{1+\xi}{1-\xi}\right)\right] u_B(\varepsilon_c + \varepsilon_i + \varepsilon_{es}). \tag{18}$$

These losses arise from the same mechanisms as those of the back wall: inelastic collisions, ion sheath losses, and electron sheath losses. However, the radial losses occur over the entire surface area of the cylindrical wall. Furthermore, the radial loss terms must account for variations in axial plasma density throughout the length of the source. The bracketed term in Eq. 18 represents the total plasma density enclosed within the radial source tube. Boundary losses occur at the thruster throat and are calculated according to

$$P_{boundary} = \frac{1}{2} e\beta n_0 u_B A_0(\varepsilon_c + \varepsilon_i + \varepsilon_{eo}). \tag{19}$$

At the throat boundary between source region and nozzle, it is again assumed that the ions reach the Bohm speed. The area of the interface is also equivalent to the cross sectional area of the thruster. Therefore, the density and area terms in the boundary power loss equation are equivalent to the expression for back wall losses. The boundary energy losses arise from inelastic collisions and acceleration of the ions to the Bohm speed. However, there is an added term for energy deposited in the nozzle, ε_{eo}. This loss takes the form:

$$\varepsilon_{eo} = 2T_e + \frac{1}{2} M_{det}^2 T_e. \tag{20}$$

As with the electron sheath loss, the first term in this expression represents the average electron energy. The second term is the energy transferred from electrons to ions via the ambipolar field that is established within the nozzle.

6. Model Outputs

Using the plasma properties of the source and the determined absorbed power, the final step in the model solution method is to evaluate the global performance metrics that the model outputs (step 4 in Fig. 3). We also include in the following a discussion of the calculated efficiency modes.

i) *Thrust*

In the context of this model, thrust generated by the ECR thruster can be expressed using the familiar form for a rocket:

$$T = \dot{m}_i v_i + (P_e - P_a) A_e, \tag{21}$$

where v_i is the velocity of ions exiting the thruster, P_e is the electron pressure at the thruster exit plane, P_a is the ambient pressure, assumed to be zero in the vacuum chamber, and A_e is the cross-sectional area included within the nozzle grazing line at the plasma detachment location. The first term represents the momentum exchange of ions exiting the thruster, and the second term is the surface force due to the effective electron pressure.

We begin examining the momentum term by defining ion mass flow rate out of the thruster. Due to continuity, the flux density of ions through the exit plane must be equivalent to the ion flux density at the thruster throat. Using the known plasma density at the throat, the ion flux density, Γ_i, can be expressed as

$$\Gamma_i = \frac{1}{2}\beta n_0 u_B A_0. \tag{22}$$

The ion mass flow rate is then the product of this ion flux density and the ion mass. The exit velocity of the ions corresponds to the velocity given by the detachment Mach number:

$$v_i = M_{det} u_B. \tag{23}$$

Substituting the definition of Bohm speed, we can simplify the first term of our thrust equation:

$$\dot{m}_i v_i = \frac{1}{2}\beta n_0 A_0 T_e e M_{det}. \tag{24}$$

Next we evaluate the thrust generated by the electron pressure. Equating ion flux at the throat and exit plane results in the relationship

$$n_e A_e = \frac{n_0 A_0}{2M_{det}}. \tag{25}$$

From this equation, we find the average electron pressure force at the exit plane using the ideal gas law. The surface force is then given by

$$P_e A_e = \frac{\beta n_0 e T_e A_0}{2M_{det}}. \tag{26}$$

Finally, we can substitute our expressions for the momentum and pressure terms, Eq. 24 and Eq. 26, into Eq. 21 to express thrust as

$$T = \frac{M_{det}^2 + 1}{2M_{det}}(e\beta n_0 A_0 T_e). \tag{27}$$

Here we neglect thrust due to neutral gas ejection, as cold gas thrust typically accounts for less than 5% of the total thrust in these devices.[12,17] Equation 27 is the thrust derived by Lafleur in the formulation of this model.[14] However, this expression does not consider the divergence of the beam, which will be present in our experimental measurements. This disparity introduces error when we regress the model outputs against experimental results (see Sec. III). To account for this, we include an additional divergence angle in our thrust equation:

$$T = \cos(\theta_D)\frac{M_{det}^2 + 1}{2M_{det}}(e\beta n_0 A_0 T_e). \tag{28}$$

In this work, we assume the characteristic divergence angle is constant at $\theta_D = 30°$. This results in a constant divergence efficiency of $\eta_D = 75\%$, which is consistent with previous experimental measurements.[3] These measurements also show that divergence efficiency varies by less than 10% across the range of operating conditions, validating our treatment of this parameter as a constant.

ii) *Specific impulse*
From thrust, we can calculate specific impulse using Eq. 2. The model is configured to take volumetric flow as SCCM, since this is the measurement used to control flow during testing. This volumetric flow rate is then converted to a mass flow rate based on the density of xenon gas at room temperature, where $1\text{SCCM} = 89.44\frac{\mu g}{s}$.

iii) *Total efficiency*
The final global performance metric output by the model is total efficiency. We note, however, that the efficiency model presented in Sec. B does not account for coupling efficiency. We control for this in comparing experimental results to the model by defining a modified model efficiency that only accounts for the power that is actually coupled into the plasma:

$$\eta^* = \frac{T^2}{2\dot{m}P_{abs}}, \tag{29}$$

where $P_{abs} = P_{back} + P_{radial} + P_{boundary}$ and $P_{abs} = \eta_{rf} P_{in}$. In practice, we have direct measurements of the input power and coupling efficiency, allowing us to determine power absorbed by the thruster. We note that in most cases, coupling efficiency approached unity (>90%).

iv) *Efficiency Modes*
From the model outputs, we extract the two efficiency modes discussed in Sec. B.2. Mass utilization is a model input, which we did not measure during our experimental testing. Instead, we learn this efficiency mode using the regression algorithm described in Sec. III. The other efficiency mode, energy efficiency, can be calculated from the model outputs and invoking Eq. 6.

III. Methods for Regression of the ECR Model

The discharge model described in Sec. II in principle allows us to calculate key performance metrics at a variety of thruster operating conditions. With that said, the model has multiple free parameters that are not known *a priori*. These inputs must be inferred by calibrating against experimental data. We describe our method for performing this inference in the following.

A. Treatment of Model Parameters

Table 1 lists the design parameters, model parameters and model outputs for the inference problem. Design parameters are treated as fixed constants that depend on the dimensions of the ECR thruster or the operating conditions being modeled. Model parameters are the properties that are being sampled and learned by our regression algorithm. These values affect the predictions made by the global discharge model and are tuned so that the model output predictions match the observed experimental data. The distributions shown in Tab. 1 for these parameters represent the range of possible values they can assume. We note here that our free model parameters capture key physical aspects of the system that we do not characterize experimentally: the degree of confinement (represented by coefficient, c), the degree of mass utilization, η_m, and the point where ions detach from the nozzle. We regress the model by comparing its outputs to experimental data.

Table 1. Discharge Model Parameter Classification

Design Parameters			
Property	**Symbol**	**Value**	**Units**
Source Radius	R_s	13.25	mm
Source Length	L_s	20	mm
Source Cross Sectional Area	A_0	5.51	cm^2
Mass Flow Rate	$\dot{m}$	1	SCCM
Coupling Efficiency	η_{rf}	$[0.6, 0.95]$	unitless
Model Parameters			
Mass Utilization	η_m	$\mathcal{U}[0, 1]$	unitless
Cross-Field Diffusion Coefficient	c	$\mathcal{U}[0, \infty)$	unitless
Detachment Mach Number	M_{det}	$\mathcal{U}[1, \infty)$	unitless
Model Outputs that are compared to data			
Thrust	T	[0.3-0.7]	mN
Absorbed Power	P_{abs}	[15-30]	W
Specific Impulse	I_{sp}	[400-750]	s

B. Model Regression with Bayesian Inference

In order to regress our model, we adopt a Bayesian approach. In this probabilistic formulation, we assume that values of the model parameters (represented symbolically as $\theta = (\eta_m, c, M_{det})$) can be described as a joint probability distribution, $P(\theta|\mathcal{D})$, that is conditioned on the model and the values of the experimentally measured data, $\mathcal{D} = (T, I_{sp}, P_{abs})$. The form for this distribution can be shown from Bayes rule to be proportional to the product:

$$P(\theta|\mathcal{D}) \propto P(\mathcal{D}|\theta)P(\theta). \tag{30}$$

Here $P(\mathcal{D}|\theta)$ is termed the likelihood and represents the probability of observing the experimental data given θ and assuming the model is correct. The prior, $P(\theta)$ represents our knowledge about the distribution of parameters before any data is observed. Provided we have forms for the likelihood and prior distributions, we can use methods like Markov Chain Monte Carlo (MCMC) to sample from Eq. 30 and thus approximate the probability distribution from the parameters.

1. Prior Distribution of ECR Model Parameters

As shown in Tab. 1, we utilize a uniform prior to bound the values of the model parameters, where the bounds are chosen to reflect the physics of the system. We first constrain mass utilization efficiency to the range of 0 to 1, since efficiencies cannot be larger than unity. We next mandate that cross-field diffusion coefficient must be positive (i.e., diffuses). Finally, we require Mach number to be greater than 1. Under the model assumption of sonic ions at the throat, a detachment Mach number less than 1 would suggest nonphysical deceleration in the nozzle. Using the uniform prior, all parameter values within the bounds are equally likely. This distribution is a comparatively "ignorant" choice, meaning that, aside from truncating the domain, our prior distribution will have minimal impact on our inferences about θ.

2. Likelihood Model

We adopt a Gaussian likelihood in this work:

$$P(\mathcal{D}_{exp}|\theta_n) = \frac{1}{2\pi^{\frac{3}{2}}|C_{\mathcal{D}}|^{\frac{1}{2}}}\exp\left(-\frac{1}{2}(\mathcal{D}_{exp}-\mathcal{D}_{model})C_{\mathcal{D}}^{-1}(\mathcal{D}_{exp}-\mathcal{D}_{model})\right). \tag{31}$$

Here $\mathcal{D}_{model} = (T_{model}, I_{sp_{model}}, P_{abs_{model}})$ and $\mathcal{D}_{exp} = (T_{exp}, I_{sp_{exp}}, P_{abs_{exp}})$ denote respectively the model predictions and experimental measurements for thrust, specific impulse, and absorbed power. $C_{\mathcal{D}}$ represents the covariance matrix that captures experimental uncertainty in these measurements:

$$C_{\mathcal{D}} = \begin{bmatrix} \Delta T^2 & 0 & 0 \\ 0 & \Delta I_{sp}^2 & 0 \\ 0 & 0 & \Delta P^2 \end{bmatrix}. \tag{32}$$

We model the uncertainty in thrust as $\Delta T = 0.03T$,which is dictated by the thrust stand we employ for this system.[17] The uncertainty in the absorbed power is a function of the measurement system and is given by $\Delta P = 0.1P$. The uncertainty in the specific impulse stems from both the thrust and flow rate measurements. We find this from propagating the error from both measurements:

$$\Delta I_{sp} = \sqrt{\left(\frac{\Delta T}{\dot{m}g}\right)^2 + \left(\frac{-T}{\dot{m}^2 g}\Delta\dot{m}\right)^2}. \tag{33}$$

We note here that in this formulation, we have assumed that the noise for each measurement is independent. In reality, there is some correlation between the uncertainty of thrust and specific impulse, which would manifest as off-diagonal elements in the covariance, $C_{\mathcal{D}}$. We have found this error to have only minor effects on the regressed results, however, and so neglect these off-diagonal terms for simplicity.

C. DRAM Sampling Algorithm

In order to sample from the posterior distribution, we employ a MCMC method based on a Gaussian random walk proposal. This technique randomly "steps" through the parameter space by proposing samples from a multivariate Gaussian distribution. We seed the sampling algorithm with an initial guess and assign a covariance matrix to our proposal distribution, which determines the step size of the random walk. However, throughout the course of the sampling algorithm, the proposal covariance matrix is adapted according to the DRAM procedure described by Haario.[18] In modifying the proposal covariance, we are able to ensure that our sampling algorithm is effectively exploring the entire sample space of model parameters.

D. Translating sampling to model outputs

Using the Bayesian regression and DRAM sampling algorithms described in Sec. B and C, we learn the model parameters that recover the experimental data at each operating condition and each wall material. For every regression point, we sample 100,000 sets of model parameters and evaluate the model using these samples. The model outputs are then compared to the experimental results using the likelihood function, and the model parameter samples that best recover the experimental values are kept. We also record the

source properties, power loss terms, model outputs and efficiency modes evaluated with the accepted model parameters. In this way, we generate distributions of these parameters across the 100,000 samples. For our later comparison between wall materials, we take the mean of these distributions, corresponding to the most probable values of these quantities of interest. In the following, we use these average values to provide a comparison between materials.

Here we have detailed the Bayesian regression algorithm used to infer model parameters, source properties, power loss terms, and model outputs. Now that we have outlined the model and the method for regressing it against data, we turn in the next section to how we generated the experimental datasets.

IV. Experimental Setup

In this section we describe the equipment used to collect experimental data. We begin by discussing the ECR thruster used in this investigation followed by details about the wall materials tested. We then outline the facility and diagnostic equipment utilized.

A. Test Article

The test article we use in this work is the University of Michigan ECR thruster II,[17] which has design elements based on the original work of ONERA.[19] The source tube is 20 mm long and 27.5 mm in diameter, with the total thruster diameter (including the propellant plenum) being 89 mm. The central antenna is machined from a graphite rod to be 20 mm long and roughly 2.25 mm in diameter. This thruster is designed to nominally operate at 30 W input power and a flow rate of 1 SCCM on xenon. The magnetic field is generated by samarium cobalt magnets and is tuned such that resonance occurs for electromagnetic waves in the microwave regime, with the nominal input frequency being 2450 MHz. The physical components of the thruster, such as the antenna, back wall and source tube, are modular to enable parametric material testing. For all experiments described in this effort, the thruster was configured with a graphite antenna and a boron nitride (BN) backwall.

1. Wall Materials Tested

To investigate the role of wall material, the thruster is outfitted with radial walls of three different materials: aluminum treated with a BN coating, graphite, and untreated aluminum. We show the thruster in these three configurations in Fig. 4.

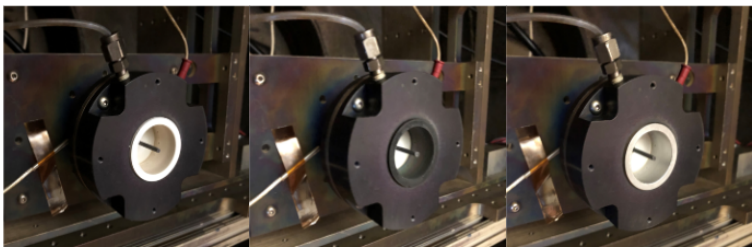

Figure 4. UM ECR thruster with boron nitride (left) graphite (center) and aluminum (right)

We chose these materials due to their varying levels of SEE. As shown in Fig. 5, we see for typical anticipated temperatures in the ECR source (e.g. 50 eV) BN walls on average emit 1.75 secondaries per incident electron, while graphite emits 0.3 secondaries per incident electron. This suggests that in the upper temperature range of the ECR source region the BN walls introduce nearly 6 times the number of secondary electrons as graphite.

B. Test Facility

We performed our experimental characterization in the Alec D. Gallimore Large Vacuum Test Facility (LVTF) at the Univeristy of Michigan's Plasmadynamics and Electric Propulsion Laboratory. LVTF is a 6 meter diameter by 9 meter long chamber, with typical background pressures the order of 10^{-7} Torr-Xe. Fig. 6 shows the test configuration of the thruster assembled in this facility.

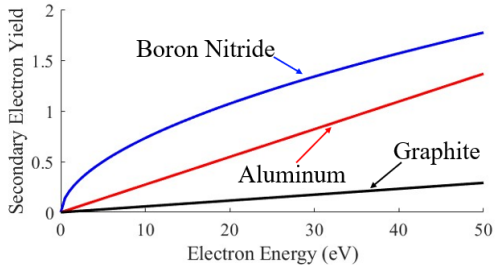

Figure 5. Secondary electron yield of examined wall materials [11,20,21]

During operation, propellant flow rate was monitored with an Alicat MCV-50SCCM flow controller. The microwave signal was generated by a Windfreak SynthHD-pro signal generator and amplified to the desired power setting by a Mini-Circuits ZHL-2425-250X amplifier. The forward and reflected power were sampled by a Mini-Circuit ZGBDC20-372HP bi-directional power coupler and measured using an Agilent P-series power meter. These components were connected to a central computer that allowed us to control propellant flow rates and input power settings. The computer also received data from the flow controller and power meter to monitor these parameters throughout the test.

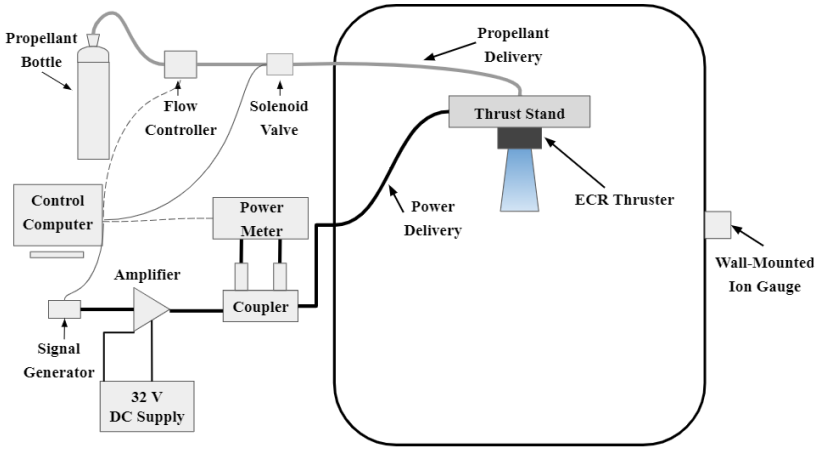

Figure 6. Test configuration of UM ECR thruster in LVTF

C. Direct Thrust Measurements

We measured the thrust force generated by the ECR thruster using a pendulum-type thrust stand developed by Wachs and Jorns,[17] which has a resolution on the order of 0.1 μN. After measuring the thrust, we calculated the other key performance metrics such as specific impulse and total efficiency according to Eq. 2 and Eq. 3, where mass flow rate and input power were measured using the configuration shown in Fig. 6.

V. Results

In this section we present the results of this investigation of wall materials. We first show the experimental data from the wall material tests. We then compare the experimental data to the results of the regressed model. Finally, we perform an efficiency breakdown using the regressed plasma properties.

A. Experimentally Measured Global Performance

Using the experimental setup described in Sec. IV, we made direct thrust measurements and calculated specific impulse and total efficiency. These data were taken for all three wall materials at a propellant flow rate of 1 SCCM and absorbed powers ranging from 15-30 W. We tested graphite more extensively at low

powers, leading to an extra data grouping at 15 W absorbed power. Figure 7 presents the thrust, specific impulse and efficiency data.

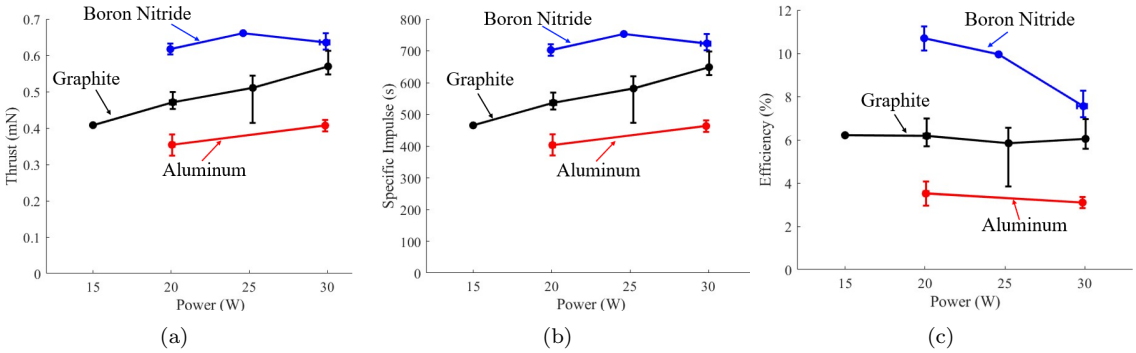

Figure 7. Experimental results for a) thrust b) specific impulse and c) total efficiency as a function of power for the ECR test article

From Fig. 7(a) and (b), we see that for all materials, thrust and specific impulse increase approximately monotonically with power. However, Fig. 7(c) shows that efficiency appears to decrease as power increases. These trends have previously been observed on other ECR test articles,[3] and have been explained in the context of changes to the mass utilization and energy efficiencies. We return to discussion of these trends in Sec. VI.A.

Additionally, these plots demonstrate a correlation between thruster performance and wall material. At a given power, the BN-coated walls yield the highest thrust, specific impulse, and efficiency. The next highest performing material tested is graphite, with aluminum resulting in the lowest performance. We further discuss the differences in global performance in Sec. VI.A.

B. Model Calibration

Armed with our experimental measurements, we next turn to performing model regression per the description in Sec. III. To this end, we first show in Fig. 8 response plots comparing the distribution of the model output to the experimental data. The points in these results represent the mean value of the distribution of model outputs. The dashed lines are the bounds that include 90% of the regressed outputs. The shaded red region represents the measurement uncertainty based on the accuracy of the experimental apparatus. The linear relationship reflected in these plots suggests agreement between experimental measurements and the model prediction within uncertainty. This validates that the model has been successfully calibrated. With this result in mind, in the next section we leverage this model as a numerical tool to assess key trends in efficiency modes with wall material.

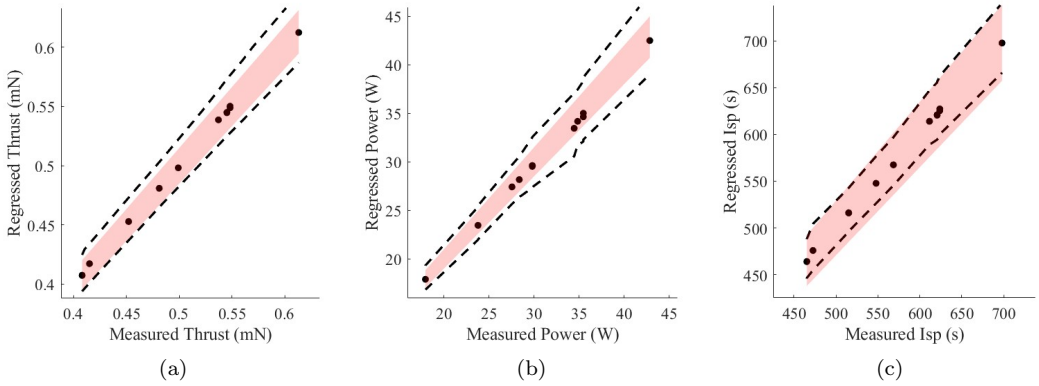

Figure 8. Comparison between calibrated model result and experimental data for a) thrust b) input Power and c) specific impulse. Data points represent the mean output value of the regressed model, the dashed black lines bound 90% of the regression samples and the red shaded area is the experimental uncertainty.

C. Modeled Efficiency Breakdown

Figure 9 shows the calculated efficiency modes of interest as a function of power for all three materials operating at 1 SCCM-Xe. We generate these results by sampling from the regressed model and averaging the output efficiency modes. We again note that we hold divergence efficiency constant at $\eta_D = 75\%$, across all operating conditions.

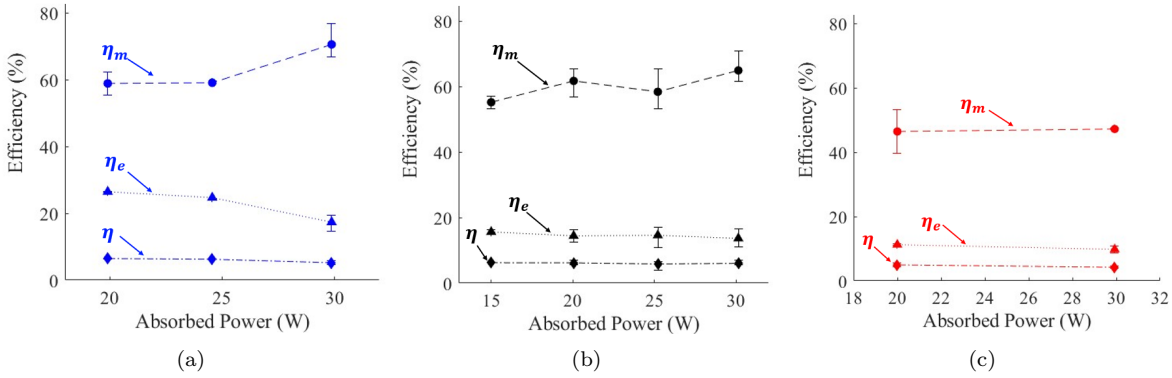

Figure 9. Efficiency modes as a function of power for a) BN b) graphite and c) aluminum

As with previous studies, we find that energy efficiency is generally 3 times lower than mass utilization, suggesting that poor energy conversion is a primary mechanism in limiting overall efficiency of ECR devices.[3,22] These plots also highlight trends in efficiency modes as a function of absorbed power. For a given flow rate, as power delivered to the thruster increases, we generally observe a slight increase in mass utilization and a decrease in energy efficiency. The relative strength of these trends appears to vary between wall materials. For a more direct comparison across materials, we next take the average over the shown power ranges from Fig. 9 and plot the modes as a function of wall material.

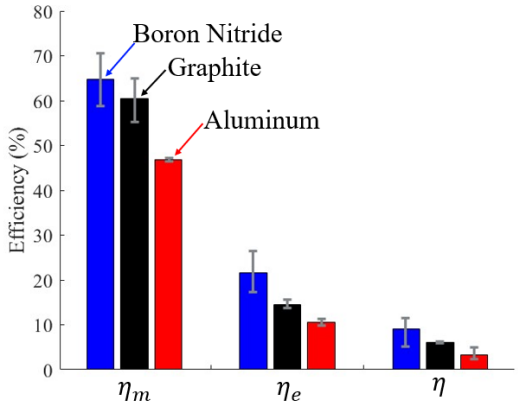

Figure 10. Average values of mass utilization, energy efficiency, and total efficiency as a function of wall material

We note from this result that the range of mass utilization (45%-70%) and energy efficiency (12%-28%) values calculated from the regressed model agree with experimentally derived efficiency breakdowns that have been published previously.[3,13,22] Fig. 10 also indicates that boron nitride walls yield an average mass utilization 5% higher than graphite and 18% higher than aluminum. Additionally, the average energy efficiency is also increased for BN: average 6% higher than graphite and 10% greater than aluminum. These results are notable in the context of the suggested role of SEE. We see that mass utilization does indeed increase, energy efficiency (a function of wall loss) does not.

Evaluation of the efficiency modes points to a combination of improved mass utilization and energy efficiency as a driving factor in the observed overall performance improvement for boron nitride walls. We comment further on the physical reasoning for these efficiency trends in Sec. VI.

VI. Discussion

In this section, we leverage our model results to discuss possible mechanisms for how SEE may explain the variation in the mass utilization and energy efficiency with wall material. We then elaborate on limitations of the present model and possible extensions.

A. The Effect of SEE on Efficiency Modes

To explain the differences in efficiency modes across the wall materials tested, we turn to previously established hypotheses and scaling laws that incorporate wall material SEE into the relevant equations. We note before proceeding that the model we adopted in this work does not explicitly allow for wall material effects. These implicitly are carried through by the variation in the model coefficients, most notably the diffusion coefficient, which we do anticipate will be modified by wall materials. A more detailed sheath model would help better elucidate the underlying trends–a step for future efforts.

1. Mass Utilization Efficiency

In order to motivate the key drivers for mass utilization, we evaluate a simplified quasi-0D scaling law for this parameter. This stems from considering the volumetric integral of the neutral continuity over the source region. From this, we approximate to first order

$$\eta_m \approx \frac{n_0 n_n K_{iz}(T_e) L A_0}{\dot{m}}. \tag{34}$$

Physically, this expression shows that as the plasma density, neutral density, and rate coefficient for ionization increase in the source, mass utilization will improve. This formulation thus translates the question of the role of wall material to a consideration of how SEE can impact these properties.

With this in mind, the neutral density in our approach is assumed to be approximately invariant with wall material as it is a function of the propellant flow rate, held constant at 1SCCM-Xe. For the plasma density, on the other hand, previous work has suggested that SEE can from the walls acts as an additional electron source term for the electrons.[2] The wall secondary electrons thus offset losses, increasing the plasma density. To examine this possibility, we show in Fig. 11 the maximum average plasma density of the source region as a function of absorbed power for each wall material. As can be seen, there is an increase in the plasma density for the BN wall in our regressed model results, particularly for higher powers. In the context of Eq. 34, this effect thus would serve to help explain the mass utilization trends.

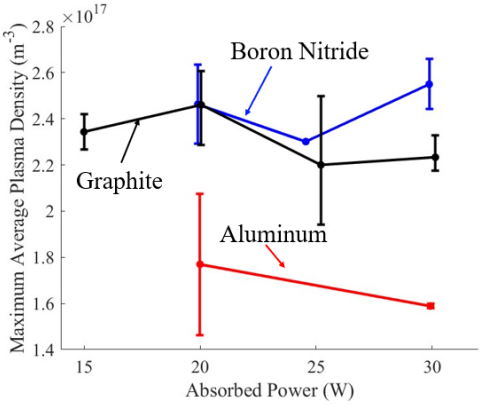

Figure 11. Maximum average plasma density as a function of absorbed power for all wall materials

With that said, another effect of the donor electrons is to potentially lower the average electron energy in the discharge. Indeed, donor electrons tend to have have lower temperatures than the primary electron population.[2] This invites the possibility that, as more of these are contributed to the source region, the average temperature of the discharge will be lowered. This decrease in electron temperature in turn will adversely impact the mass utilization. To examine this hypothesis, we show in Fig. 12 the electron temperature as

a function of power for the different wall materials as inferred from the calibrated model. This result does indeed show that the electron temperature is lower with higher SEE material.

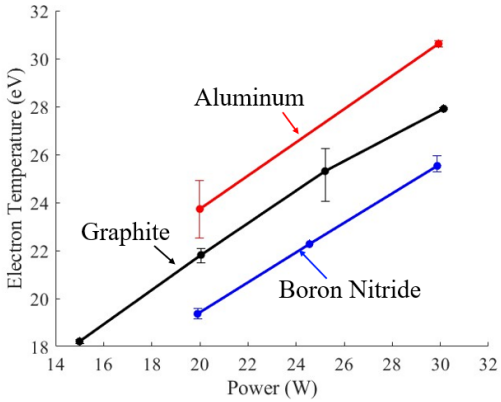

Figure 12. Electron temperature as a function of absorbed power for all wall materials

We note that these trends in density and temperature have previously been observed experimentally in tests with a miniaturized ECR gridded ion thruster.[23] In one study, a comparison was made between the device operating with low SEE, molybdenum, and comparably high SEE, alumina, walls. In each case Langmuir probe measurements were taken within the ECR source region. The results indicated an increased plasma density and lowered electron temperatures for the tests with alumina walls. Although this micro-ECR ion thruster operates at less than $\frac{1}{10}$ the propellant flow rate and power to our test article, these experimental results serve as preliminary support for our conjectures we have made informed by our model regression.

In the context of Eq. 34, the opposite trends in density and temperature with wall materials have disparate effects on the mass utilization. This invites the question as to which is the key driver. To evaluate this, we show in Fig. 13 the scaling of the effective ionization mean free path for neutrals, $\lambda_{iz} \propto 1/(n_p k_{iz}(T_e))$ extracted from our regressed model results. We observe that at low powers, graphite actually has a smaller ionization mean free path than BN. This is consistent with our results in Fig. 9, where at 20 W, graphite has a higher mass utilization efficiency. However, as power increases, BN generally has the smallest ionization mean free path, suggesting that more neutrals will be ionized before exiting the source region. This trends qualitatively with our findings for mass utilization as a function of power and wall material. The key implication thus appears to be that, at high power levels (>25 W), SEE serves to increase the plasma density, resulting in improved ionization in the source region. In this way, higher SEE materials appear to have a pronounced effect on mass utilization by acting as an electron source and increasing plasma density. We also note that this observation is consistent with the hypothesis that SEE may assist in preventing electron starvation in the source region.

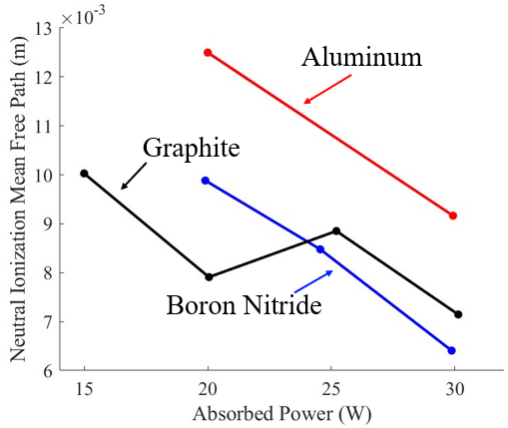

Figure 13. Ionization mean free path as a function of power for all wall materials

2. *Energy Efficiency*

Another key way that wall materials are known to influence the energy efficiency is through modifications to the plasma sheath potential. These changes can have direct implications for the wall losses. Indeed, as shown by Hobbs and Wesson, the sheath potential is altered by SEE [16]

$$\phi_s \approx -T_e \ln\left(\sqrt{\frac{m_i}{2\pi m_e}}(1-\gamma)\right), \tag{35}$$

where γ is the wall-specific SEY. From this equation, it is evident that increasing SEE lowers the magnitude of the sheath potential drop. A lessened potential drop across the sheath in turn functionally allows electrons to more readily reach the walls. This results in higher electron wall flux and higher power losses to the walls. This power loss contribution can described (c.f. Ref. 11)

$$P_{wall} \propto n_w u_B A_w \left(\sqrt{\frac{m_i}{2\pi m_e}}\exp\left(\frac{\phi_s}{T_e}\right) + (\frac{1}{2} - \frac{\phi_s}{T_e})\right), \tag{36}$$

where n_w is the plasma density at the wall and A_w is the area of the wall.

To explore this potential effect on our modeled system, we show in Fig. 14 the different contributions to the wall power loss in Eq. 36. These include the potential drop across the sheath and the plasma density at the wall, calculated here as $n_w = n_0 h_r$.

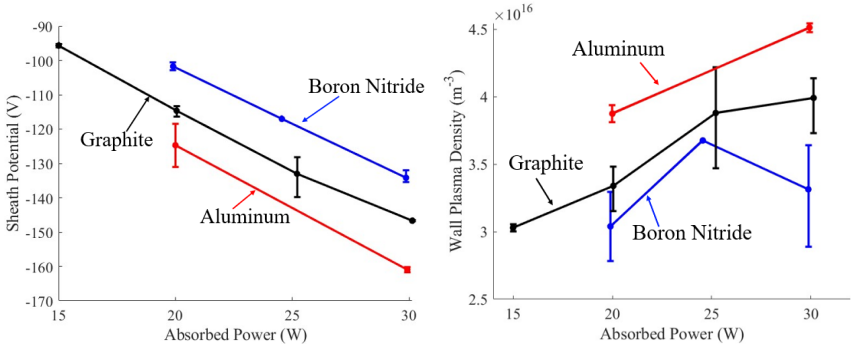

Figure 14. a) Sheath potential drop and b) plasma density at the radial wall as function of power for all wall materials

Figure 14(a) does indeed reflect a lower potential drop across the sheath (lessened magnitude sheath potential) for high SEE wall material. However, examining Fig. 14(b), we find that the plasma density at the radial wall is lowest for BN. This is the case despite the fact that Fig. 11 indicates a higher average plasma density for the BN test article. This discrepancy can be resolved by considering cross-field diffusion. Figure 15 shows the edge-to-center density ratio as a function of power for each wall material.

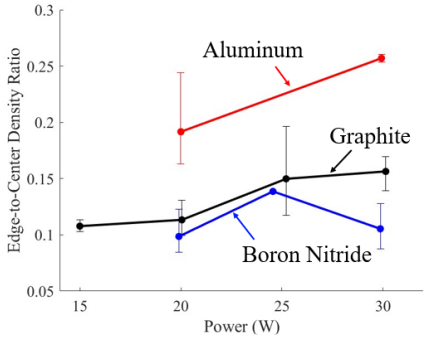

Figure 15. Edge-to-center density ratio as a function of absorbed power for each wall material

From this plot, we see that, although the average plasma density is higher for BN, it also has the lowest edge-to-center ratio. As a result, BN has a lower plasma density at the wall. This suggests that cross-field diffusion is lessened within the source region of the BN test article. We discuss a potential physical reasoning for the improved plasma confinement observed in the BN test article in Sec. B.2.

The results shown in Fig. 14, suggest opposing trends that influence energy efficiency. To determine which behavior dominates, we examine each of the power loss terms discussed in Sec. 5. Figure 16 shows the average normalized power losses to the radial wall, back wall, and throat boundary as a function of wall material.

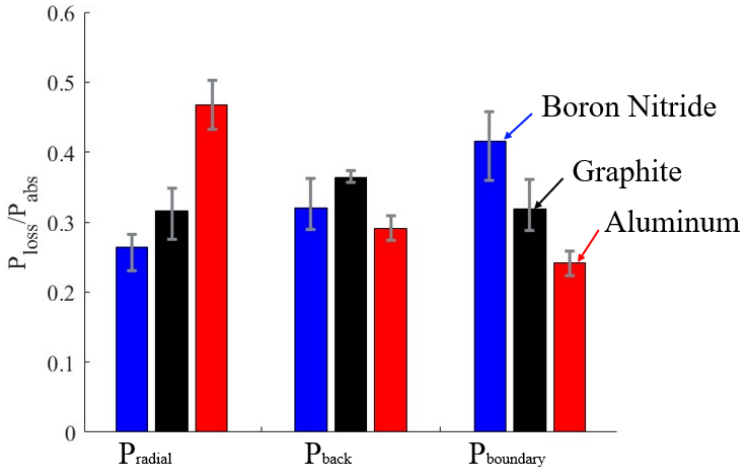

Figure 16. Average normalized power loss as a function of wall material

These results show that the radial wall losses for the higher SEE material, BN, are actually lower than the other two wall materials. This finding suggests that the increased plasma confinement (decreased edge-to-center ratio) for BN serves to limits power losses to the radial wall. This increased confinement appears to dominate over the modified sheath potential drop. Furthermore, this result is consistent with our efficiency mode analysis from Fig. 10, which showed that energy efficiency was indeed higher with BN. Not only do we observe decreased radial wall losses for the BN test article, but we also find that BN deposits more power into the nozzle boundary. This suggests that a higher fraction of power is coupled to the ions in the magnetic nozzle when operating with BN walls, which also supports our observed increased energy efficiency.

B. Limitations

In this section we discuss the limitations to this investigation. We begin by discussing shortcomings of the model used in this work and conclude with a brief examination of wall conductivity effects.

1. Model Limitations

Although the global discharge model we adopt in this work provides insight into properties of the plasma, there are several effects that are not captured by the model.

As discussed above, SEE results in modifications to the electron continuity equation by introducing an additional source term, and the source power balance by modifying the loss to the walls. The model used in this work does not account for these changes in any way. Despite this limitation, we have attempted to capture the effects of wall SEE by varying model parameters that govern physical processes within the source region that may be affected by donor electrons. By regressing these model parameters against experimental measurements with differing wall materials, we are able to approximate changes to the plasma dynamics of the source region between operating conditions. With that being said, it is possible that factors other than SEE may vary between wall materials and account for some of the trends highlighted in the regressed parameters.

2. Wall Conductivity Considerations

In this work we focus primarily on the effects of wall SEE on the plasma physics within the ECR source region. However, electrical conductivity of the walls also likely has an effect on thruster performance. It has been established that the conductivity of the walls fundamentally changes the diffusive behavior of the plasma in the source region.[24,25] With insulating wall materials, the flux of ions must be equal to the flux of electrons at every point along the wall. This condition implies that cross-field diffusion is limited to local ambipolar effects. However, if charge can be transported through the wall itself, it is only necessary to maintain global net zero current, allowing for ambipolar diffusion to be "short circuited" by localized regions of high diffusion, enhancing losses to the walls. This suggests that insulating walls may serve to reduce radial wall losses and increase source plasma density, thereby improving mass utilization. These proposed effects are indeed observed in our model results for edge-to-center density ratio, mass utilization, and power loss terms as shown in Figs. 15, 10 and 16, respectively.

To this point, in this study, we tested two conductive materials (aluminum and graphite) and only one insulator (boron nitride). Viewed through SEE, boron nitride had the highest SEY and yielded the highest performance. However, between the two conductive materials, aluminum has higher SEY than graphite but displayed worse performance, suggesting no clear trend in performance with SEY. In contrast, we note that aluminum is approximately 1000 times more conductive than graphite,[26] and hence performance increased monotonically with decreasing conductivity. This suggests that wall conductivity effects may be an equally, if not more important influence on overall behavior of ECR thrusters than SEE and warrants investigation in the future.

VII. Conclusion

We presented in this work experimentally measured global performance metrics for an ECR thruster operating with boron nitride, graphite and aluminum radial walls. We then regressed a global discharge model against the experimental results to gain insight into the unmeasured plasma properties such as electron temperature and plasma density. Using the plasma properties determined by the regression algorithm, we performed an efficiency breakdown, examining mass utilization and energy efficiency across the three materials. The experimental results showed a factor two increase in specific impulse and a factor three increase in total efficiency when comparing the lowest performing material, aluminum, and the highest performing material, BN. The efficiency breakdown indicated that mass utilization resulting from BN walls is greater by an average of 18% over aluminum and 5% over graphite. We attributed the improved mass utilization to increases in both plasma density and source residence time of electrons with BN walls. Larger energy efficiencies were also observed with BN, averaging 6% higher than graphite and 10% higher than aluminum. Examination of the source power balance illustrated that BN, has a reduction in power lost to the radial wall compared to the other materials. We explained this behavior in the context of changes to the sheath potential and the plasma density at the wall. It was found that the BN test article better confined the plasma, resulting in lower plasma density at the wall and lower wall losses. Wall conductivity was proposed as a potential physical explanation for the improved confinement. Additionally, we found that BN imparts more power to the boundary of the magnetic nozzle, resulting in more energy coupled to the ions.

To gain more insight moving forward, it will be necessary to modify the global discharge model. This will include accounting for wall SEE in the electron continuity equation, as well as the modified sheath potential in the power balance. Furthermore, it will be informative to experiment with a wider variety of insulating wall materials. By modifying the model and collecting experimental data for multiple insulators with varying SEY, we will be able to more effectively decouple the effects of SEE from wall conductivity in the ongoing effort to better characterize and improve performance of ECR thrusters.

VIII. Acknowledgements

This work was supported by the Air Force Office of Scientific Research Space Power and Propulsion Program. The authors would like to thank Collin Whittaker, Declan Brick, Parker Roberts, and Dr. Tate Gill for many useful discussions.

References

[1] Chen, F. F., *Introduction to Plasma Physics and Controlled Fusion*, Springer International Publishing, 2016.

[2] Geller, R., *Electron Cyclotron Resonance Ion Sources and ECR Plasmas*, Institute of Physics Publishing Bristol and Philadelphia, 1996.

[3] Vialis, T., Jarrige, J., Packan, D., and Aanesland, D., "Direct Thrust Measurement of an Electron Cyclotron Resonance Plasma Thruster," *Journal of Propulsion and Power*, 2018, pp. 1–11. URL `https://hal.science/hal-01849176/document`.

[4] Boni, F., Jarrige, J., Desangles, V., and Minea, T., "The curling probe: A numerical and experimental study. Application to the electron density measurements in an ECR plasma thruster," *Review of Scientific Instruments*, Vol. 92, No. 033507, 2021.

[5] Crimi, G. F., "Investigation of a Microwave Generated Plasma in a Non-Uniform Magnetic Field," Ph.D. thesis, University of Pennsylvania, 1967.

[6] Hepner, S. T., "The Influence of Instabilities on the Electron Dynamics of a Magnetic Nozzle," Ph.D. thesis, University of Michigan, 2022.

[7] Ahedo, E., and Merino, M., "On Plasma Detachment in Propulsive Magnetic Nozzles," *Physics of Plasmas*, Vol. 18, No. 053504, 2011.

[8] Hooper, E., "Plasma Detachment from a Magnetic Nozzle," *Journal of Propulsion and Power*, Vol. 9, No.5, 1993.

[9] Moses, R. W., Gerwin, R. A., and Schoenberg, K. F., "Resistive plasma detachment in nozzle based coaxial thrusters," *American Institute of Physics*, 1992.

[10] Arefiev, A. V., and Breizman, B. N., "Magnetohydrodynamic scenario of plasma detachment in a magnetic nozzle," *Physics of Plasmas*, Vol. 12, 2005.

[11] Goebel, D. M., and Katz, I., *Fundamentals of Electric Propulsion: Ion and Hall Thrusters*, JPL Space Science and Technology Series, 2008.

[12] Peterschmitt, S., "Development of a Stable and Efficient Electron Cyclotron Resonance Thruster with Magnetic Nozzle," Ph.D. thesis, Institut Polytechnique De Paris, 2020.

[13] Sheppard, A. J., and Little, J. M., "Performance Analysis of an Electron Cyclotron Resonance Thruster with Various Propellants," *Journal of Propulsion and Power*, Vol. 38, No. 6, 2022, pp. 998–1007. https://doi.org/10.2514/1.B38698.

[14] Lafleur, T., "Helicon Plasma Thruster Discharge Model," *Physics of Plasmas*, Vol. 21, 2014. https://doi.org/10.1063/1.4871727.

[15] Hayashi, M., "Determination of electron-xenon total excitation cross-sections, from threshold to 100 eV, from experimental values of Townsend's α," *Journal of Physics D: Applied Physics*, 1983.

[16] Hobbs, G. D., and Wesson, J. A., "Heat Flow through a Langmuir Sheath in the Presence of Electron Emission," *Plasma Physics*, Vol. 85, 1967, pp. 85–87.

[17] Wachs, B. N., "Optimization and Characterization of Facility Effects for a Low Power Electron Cyclotron Resonance Magnetic Nozzle Thruster," Ph.D. thesis, University of Michigan, 2022.

[18] Haario, H., Laine, M., Mira, A., and Saksman, E., "DRAM: Efficient Adaptive MCMC," *Statistics and Computing*, Vol. 16, 2006, pp. 339–354.

[19] Jarrige, J., Elias, P.-Q., Cannat, F., and Packan, D., "Performance Comparison if an ECR Plasma Thruster using Argon and Xenon as Propellant Gas," *33rd International Electric Propulsion Conference*, 2013.

[20] Baglin, V., Bojko, J., Grobner, O., Henrist, B., and N, H., "The Secondary Electron Yield of Technical Materials and its Variation with Surface Treatments," *EPAC 2000, Vienna, Austria*, 2000.

[21] Cazaux, J., "Secondary Electron Emission Yield: Graphite and some Aromatic Hydrocarbons," *Journal of Physics D: Applied Physics*, Vol. 38, No. 14, 2005, pp. 2443–2445. https://doi.org/10.1088/0022-3727/38/14/021.

[22] Peterschmitt, S., and Packan, D., "Comparison of Waveguide Coupled and Coaxial Coupled ECRA Magnetic Nozzle Thruster using a Thrust Balance," *36th International Electric Propulsion Conference*, 2019.

[23] Meng, S. F., Zeng, D. M., Zhu, X. M., and Yu, D. R., "Wall material effects in a minimized electron cyclotron resonance ion thruster," *Acta Astronautica*, Vol. 219, 2024. https://doi.org/10.1016/j.actaastro.2023.12.034.

[24] Drentje, A., Wolters, U., Nadzeyka, A., Meyer, D., and Wiesemann, K., "Simon short circuit effect in ECRIS," *Review of Scientific Instruments*, Vol. 73, No. 2, 2002, pp. 516–520. https://doi.org/10.1063/1.1429315.

[25] Simon, A., "Ambipolar Diffusion in a Magnetic Field," *Physical Review*, Vol. 90, No.2, 1955.

[26] Haynes, W., Lide, D. R., and Bruno, T. J., *CRC Handbook of Chemistry and Physics*, Taylor and Francis Group, 2014.